Deducing non-migrating diurnal tides in the middle thermosphere with GOLD observations of the Earth's far ultraviolet dayglow from geostationary orbit

Christopher S. Krier[1], Scott L. England[1], Katelynn R. Greer[2], J. Scott Evans[3], Alan G. Burns[4], and Richard W. Eastes[2]

[1]Aerospace and Ocean Engineering, Virginia Polytechnic Institute and State University, Blacksburg, VA, USA
[2]Laboratory for Atmospheric and Space Physics, University of Colorado Boulder, Boulder, CO, USA
[3]Computational Physics, Inc., Springfield, VA, USA
[4]High Altitude Observatory, National Center for Atmospheric Research, Boulder, CO, USA

Corresponding author: Christopher S. Krier (ckrier@vt.edu), ORCID: 0000-0002-3786-4094

Key Points:

i. Novel technique for deducing non-migrating tides in concurrent observations of temperature and composition.
ii. First observations of non-migrating diurnal tides from an observational platform in geostationary orbit using GOLD.

iii. During both October 2018 and January 2020, there are differences between the tidal structure in TIE-GCM simulations and the GOLD dataset.

Abstract

The Global-scale Observations of the Limb and Disk (GOLD) Mission images middle thermosphere temperature and the vertical column density ratio of oxygen to molecular nitrogen ($\Sigma O/N_2$) using its far ultraviolet imaging spectrographs in geostationary orbit. Since GOLD only measures these quantities during daylight, and only over the ~140º of longitude visible from geostationary orbit, previously developed tidal analysis techniques cannot be applied to the GOLD dataset. This paper presents a novel approach that deduces two specified non-migrating diurnal tides using simultaneous measurements of temperature and $\Sigma O/N_2$. DE3 (diurnal eastward propagating wave 3) and DE2 (diurnal eastward propagating wave 2) during October 2018 and January 2020 are the focus of this paper. Sensitivity analyses using TIE-GCM simulations reveal that our approach reliably retrieves the true phases, whereas the restriction in longitude and random noise can lead to ~ 50% error in the retrieved amplitudes at certain latitudes. Application of our approach to GOLD data during these time periods provides the first observations of non-migrating diurnal tides in measurements taken from geostationary orbit. We identify discrepancies between GOLD observations and TIE-GCM modeling. It is found that ionospheric contamination of $\Sigma O/N_2$ perturbations vary with season and can introduce biases as large as 3% around the equatorial ionization anomaly.

Plain Language Summary

The uppermost region of the Earth's atmosphere, known as the thermosphere (~80-600 km altitude), is connected to the lowermost region by planetary-scale atmospheric waves, called non-migrating tides, which are thermally driven and do not follow the apparent motion of the Sun across the sky. Understanding non-migrating tides is essential to describing the global dynamics of the Earth's upper atmosphere. There is a gap in observations of these waves in the middle thermosphere temperature, around 150 km altitude. The NASA/GOLD instrument, in geostationary orbit above the mouth of the Amazon River, images the temperature and composition of the middle thermosphere. Conventional tidal analysis techniques cannot be applied to the GOLD dataset, so we have designed a novel technique that infers important tides using simultaneous measurements of temperature and composition. For two separate time periods, we apply our technique to simulated observations and actual GOLD data. We find that our technique generally infers the most important tides in simulated data with high accuracy. The GOLD data reveal valuable observations of tides in the middle thermosphere as well as discrepancies with the simulated data.

1) Introduction

The temperature and composition of the middle thermosphere change drastically with altitude. The neutral temperature increases sharply with altitude while the density of neutral constituents tends to decrease exponentially according to their respective scale heights (as well as the production and loss mechanisms for certain species). Atomic oxygen and molecular nitrogen are the two main constituents of this region. The vertical column density ratio of these two ($\Sigma O/N_2$) is a sensitive measure of thermosphere composition. Any upward propagating waves present in the mesosphere/lower thermosphere (MLT) can impact middle thermosphere temperature and composition structures. A subset of thermal atmospheric tides, including some non-migrating components, are generated in the troposphere and have long enough vertical wavelengths to penetrate the thermosphere (Hagan et al., 2002). Decades of space-based measurements have shown that the upper atmosphere owes a significant amount of its longitudinal variability to non-migrating tides (e.g., Forbes et al., 2003, 2008; García-Comas et al., 2016; Häusler & Lühr, 2009; Lieberman, 1991, 2013; Oberheide et al., 2002).

Thermal atmospheric tides are persistent planetary-scale waves in the neutral atmosphere which are principally forced by absorption of solar radiation. They have components which have periods that are subharmonics of a solar day and zonal wavelengths that are integer fractions of circles of constant latitude. Non-migrating diurnal tides are the non-Sun-synchronous components that have periods equal to a solar day. These tidal components induce longitudinal and local time perturbations in the thermosphere-ionosphere system, and it has been shown that some of the most prominent are forced by latent heat release from deep tropical convection in the equatorial troposphere (Hagan et al., 2007). Additional sources of these waves in the thermosphere include, but are not limited to, changes in solar radiation absorption by the troposphere (Zhang et al, 2010a), wave-wave interactions (Forbes et al., 2006), and magnetic field influences (Jones et al., 2013). Non-migrating diurnal tides perturb the MLT neutral temperature (Zhang et al., 2006), thermospheric wind (Liebermann et al., 2013), neutral composition (Oberheide et al., 2013), and significantly modify the ionosphere (England et al., 2012; Immel et al., 2006). Accurate characterization of non-migrating tides is required to establish agreement between modeled and observed longitudinal variations of thermosphere dynamics (Ward et al., 2010). At a constant latitude and altitude, a tidal component with period

n and zonal wavenumber s induces a perturbation in universal time t and longitude λ of the form, following Zhang et al., (2006),

$$A_{n,s}\cos\left(n\Omega t + s\lambda - \phi_{n,s}\right) \tag{1}$$

Where $s < 0$ denotes eastward zonal propagation, Ω is the rotation rate of the Earth, $A_{n,s}$ is the tidal component's amplitude, and ϕ is the tidal component's phase (typically defined as the universal time of maximum at 0º longitude). It is commonplace to analyze spacecraft measurements in the local time frame. The conversion between local time t_{LT} and universal time t is the following:

$$t_{LT} = t + \lambda/\Omega \tag{2}$$

Substituting Eqn. 2 into Eqn. 1 yields the tidal perturbation in the local time frame:

$$A_{n,s}\cos\left(n\Omega t_{LT} + (s-n)\lambda - \phi_{n,s}\right) \tag{3}$$

Migrating tides ($n = s$) are thus longitudinally invariant at a constant local time while non-migrating ($n \neq s$) control longitudinal variability in the local time frame. Evidently, viewing a tidal component in the local time frame Doppler shifts its zonal wavenumber because of viewing the tidal component in a reference frame that is rotating westward relative to the universal time frame. The naming convention of tidal components used in this paper is as follows. The name of a tidal component begins with its period: (D = diurnal, S = semidiurnal, T = terdiurnal), followed by its horizontal propagation direction: (E = eastward, W = westward, no letter included in the case of stationary wave), and ends with its zonal wavenumber in the universal time frame. For example, DE3 is the tidal component that propagates eastward with diurnal period and zonal wavenumber 3 and S0 is the stationary semidiurnal component.

Longitudinal oscillations caused by non-migrating diurnal tides can be found in various atmospheric fields observed by spacecraft. The global longitude coverage afforded by continuous datasets collected by low Earth orbiting satellites enables the decomposition of observed tides into zonal wavenumbers. The SABER temperature dataset, collected by TIMED in low Earth orbit, has elucidated the climatology of tides in the MLT region (Forbes et al., 2008; Zhang et al., 2006). Non-migrating tides have been characterized in zonal wind at 400 km as observed by CHAMP (Haüsler and Lühr, 2009) as well as near 260 km by GOCE (Gasperini et al., 2015). Consequently, the tidal spectrum of the MLT is well-understood on climatological timescales and there is some knowledge of tides at the upper thermosphere, but there exists a gap of understanding of tidal temperature dynamics in the middle thermosphere. DE3 has been identified as the dominant tidal component at around September equinox (Forbes et al., 2006; Haüsler and Lühr, 2009). Upward propagating tides, such as DE3 and DE2, are forced in the tropical troposphere and obtain their greatest amplitudes in the tenuous upper atmosphere as a result of conservation of energy. Tidal dissipation is expected to play a role in the middle thermosphere where molecular diffusion and ion drag become more important. Up to now, empirical modeling, namely, CTMT (Oberheide et al., 2011), has been used to extend MLT temperature tides to the middle thermosphere. Recently, Nischal et al. (2019) diagnosed non-migrating tides in nitric oxide 5.3 μm and carbon dioxide 15 μm infrared cooling rates between 100 and 150 km as measured by SABER. Infrared cooling rate tides derived from SABER are a sensible proxy for tidal activity in middle thermosphere temperature. However, characterization of tides in middle thermosphere temperature has not been done heretofore due to the absence of global-scale systematic measurements. Tidal features are expected to be prominent in spacecraft measurements of daytime $\Sigma O/N_2$, but such variations have not yet been fully explained at all local times (He et al., 2010; Kil et al., 2013). As discussed in Cui et al. (2014), the linearized continuity equation for plane wave perturbations in the absence of rapid diffusion and in the long-wavelength limit takes the form

$$\frac{\tilde{\rho}_i}{\bar{\rho}_i} = \frac{j\tilde{w}}{\omega H_i}, \tag{4}$$

Where $\tilde{\rho}_i/\bar{\rho}_i$ is the relative density perturbation corresponding to species i, $\tilde{w}$ is the vertical wind perturbation, ω is the wave period, H_i is the species-dependent scale height, and j is the imaginary unit. Therefore, atomic oxygen and molecular nitrogen respond differently according to their respective scale heights. Modification of the distribution of atomic oxygen and molecular nitrogen in the thermosphere is one pathway through which tides can modify the ionosphere (England et al., 2010) since the ion production rate is proportional to [O] while ionosphere loss is proportional to [N_2]. Analysis of TIMED/GUVI data (He et al., 2010) revealed unexpected wavenumber-4 longitudinal signatures in $\Sigma O/N_2$ which remained stationary. This contradicts the expectation from previous tidal observations that wavenumber-4 variations propagate eastward due to DE3 and SE2. Kil and Paxton (2011) and Kil et al. (2013) proposed that 135.6 nm emissions originating from O+ radiative recombination in the ionosphere contribute more to the tidal variations in the derived $\Sigma O/N_2$ as compared to contributions from emissions due to photoelectron impact in the middle thermosphere. In Section 4, we discuss possible ionospheric signatures in the GOLD measurements of $\Sigma O/N_2$ used in this work.

The importance of properly characterizing troposphere-thermosphere tidal coupling has partially motivated the dedication of several novel spaceflight missions designed to investigate the thermosphere and ionosphere from Earth orbit. The NASA Global-scale Observations of the Limb and Disk (GOLD) mission has been imaging neutral temperature and $\Sigma O/N_2$ from geostationary orbit since October 2018 (Eastes et al., 2020). The global and continuous sampling afforded by GOLD allows for the study of tides at periods much shorter than the precession period of a low Earth orbiting spacecraft. However, the GOLD instrument only samples on the dayside disk within its field-of-regard. Therefore, the full tidal spectrum cannot be extracted from the GOLD dataset. This paper presents a novel method which deduces dominant non-migrating diurnal tides from concurrent GOLD measurements of neutral temperature and $\Sigma O/N_2$. The methodology outlined in this paper can be adapted to any remote sensing mission from geostationary orbit measuring both temperature and composition.

The purpose of this paper is to (1) describe a novel approach to deducing non-migrating diurnal tides using observations of far ultraviolet dayglow from geostationary orbit and (2) present first results from application of the approach to GOLD data. This paper is organized as follows. Section 2 describes the GOLD and TIEGCM datasets used in this work. Section 3 provides an explanation of the non-migrating diurnal tide retrieval algorithm. Section 4 presents tests of the method on simulated GOLD data as well as the first tides retrieved from GOLD data during two seasons, focusing on DE3 and DE2. Section 5 gives a summary and conclusions.

2) Data

2.1 GOLD Dayside Disk Observations

The GOLD mission employs two identical far ultraviolet imaging spectrographs onboard the SES-14 telecommunications satellite in geostationary orbit at 47.5º West (McClintock et al., 2020a; McClintock et al., 2020b). From geostationary orbit, GOLD has the advantage of being able to separate spatial and temporal variations as well as image the Earth without being contaminated by the South Atlantic Anomaly. The two identical and independent channels (A and B) of the GOLD instrument measure emissions from ~ 132 to 162 nm of the limb and disk in its field-of-regard which encompasses much of North and South America, the Atlantic Ocean, and West Africa. GOLD performs dayside disk scans ~ 68 times each day at 30-minute cadence. The northern and southern hemispheres are scanned separately. GOLD infers disk neutral temperature from the rotational structure of N_2 LBH band system emissions, ~2/3 of which comes from within one scale height of the altitude of peak emission near 150 km. The GOLD disk neutral temperature is thus an effective, column integrated quantity that is weighted heavily by the peak of the N_2 LBH volume emission rate (photons cm^{-3} s^{-1}). Since the peak altitude of emission increases with solar zenith angle (SZA) and neutral temperature increases rapidly with height, there is a weak (<20%) dependence of the GOLD effective temperature on SZA, particularly above ~60°. GOLD infers $\Sigma O/N_2$ from atomic oxygen 135.6 nm and molecular nitrogen LBH band emissions (Correira et al., 2020). Disk temperature and $\Sigma O/N_2$ are not retrieved when the SZA is greater than 80° or the view angle from local nadir, referred to as the emission angle, is greater than 75°. From geostationary orbit, GOLD provides new opportunities to investigate the impacts of neutral dynamics (Oberheide et al., 2020) and geomagnetic activity (Cai et al., 2020; Cai et al., 2021) on thermospheric composition. One of the primary scientific objectives of the GOLD mission is to determine the significance of tides propagating from below on the thermospheric temperature structure (Eastes et al., 2017). This work addresses this objective by deducing non-migrating diurnal tides in the combined temperature-composition dataset from GOLD. In the following, we use GOLD Level 2 TDISK and ON2 data products, Version 3, which both use channel A exclusively and contain images with data reported at 52 longitudes and 46 latitudes (250 x 250 km^2 resolution at nadir).

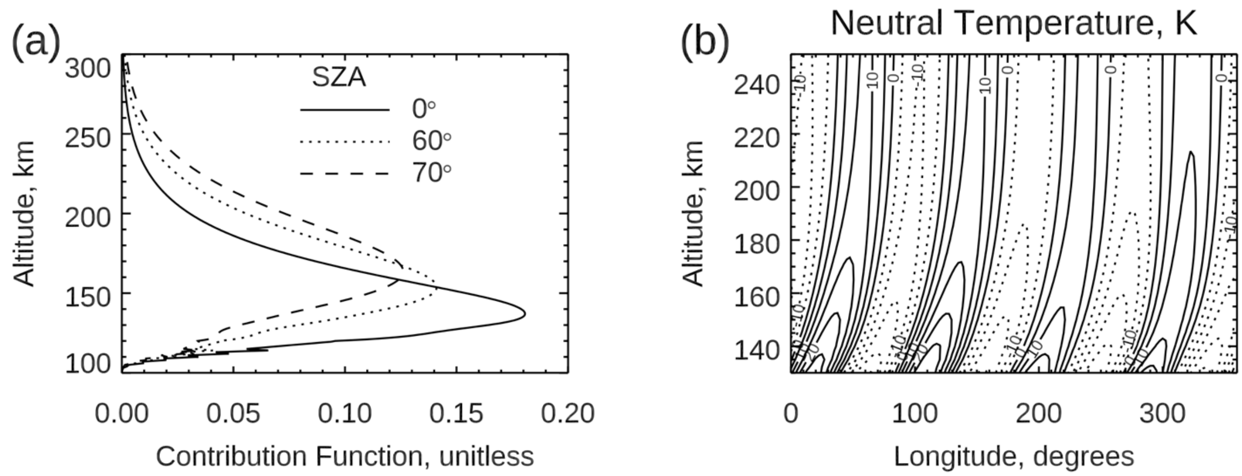

Figure 1. *(a) Contribution function used in the computation of effective neutral temperature at three select solar zenith angles for nadir viewing. (b) TIE-GCM non-migrating diurnal temperature field as a function of altitude and longitude at 12:00 LT during October.*

2.2 TIE-GCM Simulation of Effective Neutral Temperature and ΣO/N_2

The NCAR Thermosphere Ionosphere Electrodynamics General Circulation Model (TIE-GCM) is a nonlinear, three-dimensional representation of the coupled thermosphere-ionosphere system (Maute et al., 2017). The TIE-GCM output used in this work has 10-minute temporal resolution and 2.5°× 2.5° spatial resolution. The 10.7 cm solar radio flux was set to 70 sfu. The lower boundary, at approximately 97 km, is perturbed by tides from the Global Scale Wave Model (Hagan et al. (2002); see also Zhang et al. (2010b) and references therein) thereby representing propagation of tides from below. As a model of the disk neutral temperature, we calculate effective neutral temperature which is given by:

$$T_n^{eff}(\lambda) = \frac{\int j(s) e^{-\tau(s,\lambda)} T_n(s) ds}{\int j(s) e^{-\tau(s,\lambda)} ds} \qquad (5)$$

Where s is the slant path distance from the spacecraft (cm), j is the N_2 LBH volume emission rate (photons cm^{-3} s^{-1}), τ is the wavelength dependent slant optical depth due to absorption by molecular oxygen, and T_n is the neutral temperature (K). For our calculations of effective temperature, we define j as that of the N_2 LBH (2,0) band at 138.3 nm. Equation 5 can be rewritten as

$$T_n^{eff}(\lambda) = \int C(s,\lambda) T_n(s) ds \qquad (6)$$

Where $C(s,\lambda)$ is a normalized emission rate profile called the contribution function which weights the neutral temperature profile. The contribution function, whose altitude dependence changes with solar zenith angle and emission angle (EMA), maximizes at the altitude of peak LBH emission rate. Figure 1a shows the contribution function for nadir viewing (EMA = 0°) and for three select solar zenith angles: 0°, 60°, and 70°. Figure 1b presents the TIE-GCM neutral temperature non-migrating diurnal field as a function of altitude and longitude at 12:00 LT during October. There is a clear wavenumber-4 pattern and eastward phase progression up to a certain point, ~ 180 km, above which there is no phase progression. This indicates the DE3 tide. The temperature amplitude of the tides at the altitude of the peak emission is on the order of 10 K, but the effective temperature amplitude is necessarily lower since a band of altitudes, over which tidal phase varies, is sampled. For our purposes, we keep the viewing geometry angles constant at SZA = 70° and EMA = 0°. This is justified because (1) our approach (discussed in Section 3) uses data at SZA ~ 70°, (2) the contribution function depends weakly on EMA at high SZA, and (3) allowing SZA to vary would lead to distorted tides due to SZA effects. To compute a $\Sigma O/N_2$ from TIE-GCM, we define the vertical O column densities relative to a standard reference N_2 depth of 10^{17} cm^{-2} (Strickland et al., 1995). The non-migrating diurnal tidal phases that are used as *a priori* information in our approach (see Section 3) are computed as a function of latitude and month using two-dimensional fast Fourier transforms. Figure 2 presents the latitudinal structure of select non-migrating diurnal tides in effective neutral temperature and $\Sigma O/N_2$ during October and solar minimum conditions according to TIE-GCM. Note that DE3 is the dominant tide during this season. Figure 3 is the same as Figure 2 but for January and solar minimum conditions. In January, DE3 and DE2 are the two leading components in the non-migrating diurnal spectrum. The tidal phases predicted by linear wave theory are not used in our approach (Section 3) because, in the middle thermosphere, where tidal dissipation becomes important and wave components may interact nonlinearly with one another, tidal structures depart substantially from linear wave theory. Therefore, numerical computation of the tides is required in the thermosphere. It is thought that TIE-GCM provides realistic temperature-composition phase relationships of the tides which strongly correspond to the horizontal wavelengths of the tides.

In Section 4.1, we use a simulated GOLD dataset to test the sensitivity of our approach to random noise and aliasing. We simulate GOLD images of neutral temperature and $\Sigma O/N_2$ by projecting the 24-hour, full global coverage, TIE-GCM model output onto the disk in the GOLD field-of-regard. This is done through a geolocation algorithm that determines the perimeter of the disk in GOLD's field-of-regard. Only model grid points inside this perimeter are sampled for our analysis and, consistent with GOLD data products, we restrict data to SZA $< 80°$ and EMA $< 75°$.

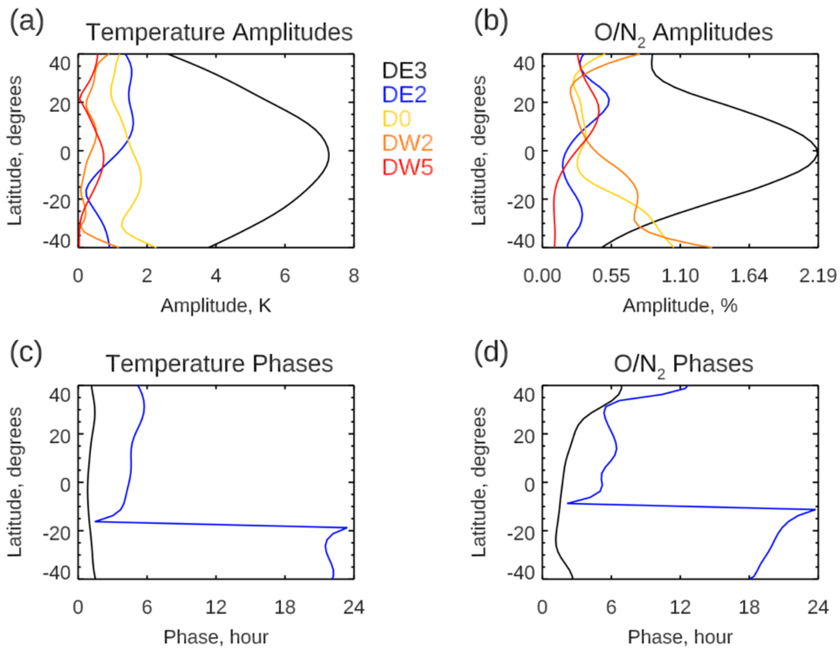

Figure 2. *TIE-GCM non-migrating diurnal tidal amplitudes and phases as a function of latitude for effective neutral temperature, (a) and (c), and column O/N_2 ratio, (b) and (d), during October and solar minimum conditions.*

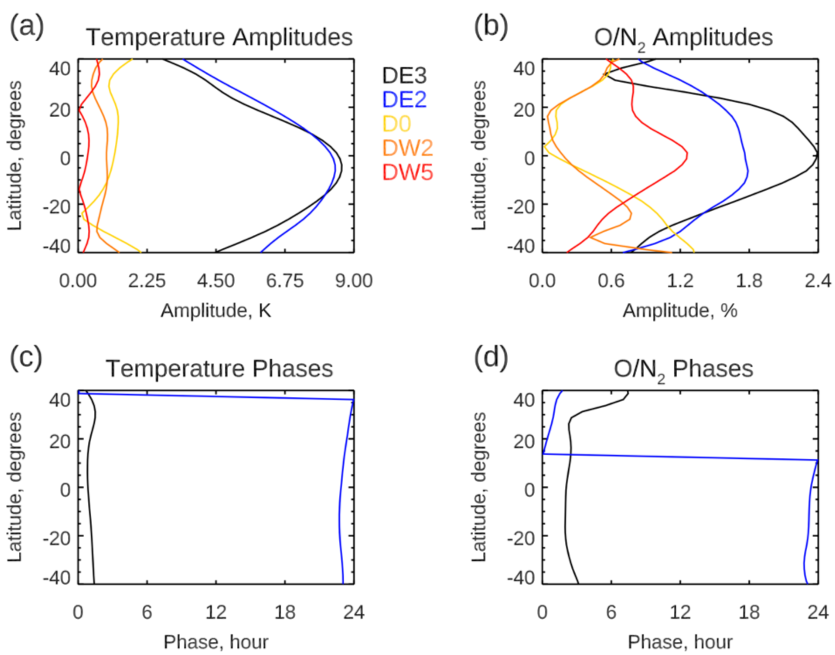

Figure 3. *Same as Figure 2 but for January.*

3) A Novel Approach to Deducing Non-Migrating Diurnal Tides

The algorithm used in this work deduces the dominant, non-migrating diurnal tides in the combined temperature-composition dataset from GOLD. The algorithm products are tidal amplitudes and phases as functions of latitude for two specified non-migrating diurnal components. Only two tides are retrieved owing to the limited longitudinal sampling from geostationary orbit and the computational expense of looking for more than two. Testing revealed that looking for a third tidal component does not improve the retrieval of the first and second tidal components in the October test case. In this section, we will describe the case of deducing the DE3 and DE2 tides during October to provide an overview of the procedure. Deducing other tides during other seasons follows a similar approach (shown in Section 4.2). The algorithm assumes that the non-migrating diurnal variations are composed of two tidal components: DE3 and DE2, in this case. The validity of this assumption is assessed in Section 4.1. A constraint on the temperature-composition phase differences extracts the correct components by enforcing consistency between the deduced temperature and composition tides whose phase relationship depend on the horizontal wavelength and direction of zonal propagation (Eqn. 4). Our algorithm makes the additional assumption that the zonal mean of the dusk – dawn difference is correct despite the incomplete longitude coverage. We have found that the DE3 amplitude bias introduced by limited longitude sampling is on average less than 2% for October and depends on the DE3 phase. For January, we found that the bias in the maximum deviation of the non-migrating diurnal proxy is on average less than 5% and depends on the tidal phases of DE3 and DE2. Because the same local times, longitudes, and latitudes are sampled each day, planetary waves should not alias into the derived tides, an advantage with analyzing observations from geostationary orbit.

A proxy for the non-migrating diurnal tides is computed in the following way. First, at each spatial grid point, we take half the difference of two measurements taken at local times roughly 12 hours apart. This removes the semidiurnal signal and leaves the diurnal signal (assuming that higher order periodicities are negligible). For dayside disk sampling from geostationary orbit, computing ~12-hour local time differences is achieved by taking the difference of measurements near dusk and dawn. We interpolate to the earliest morning local time and the latest evening local time possible to take the maximum constant local time difference. Additionally, we require that the SZA for the dusk and dawn data points are within 1 degree because offsets in SZA would introduce large biases (Figure 1a). This requirement typically leads to data being analyzed at SZA ~ 70°. The non-migrating diurnal proxy at each latitude bin is then specified by the deviations from the zonal mean of the dusk – dawn differences. For each latitude, the method of analysis proceeds by normalizing the longitudinal perturbations. For temperatures, this is done by dividing by the maximum temperature perturbation M_T, i.e., the maximum deviation from the zonal mean of the dusk – dawn differences. Similarly, for $\Sigma O/N_2$, this is done by dividing by the maximum $\Sigma O/N_2$ perturbation M_{R}. In this way, temperature and $\Sigma O/N_2$ are weighted evenly in the fit. The normalized longitudinal perturbations serve as the observations to be fitted to in a least squares approach. It is important to note that GOLD affords approximately 10-hour local time differences rather than the ideal 12-hour because of the SZA restrictions. Therefore, when least squares fitting, we use tidal basis functions which include correction terms accounting for the less than 12-hour local time differences following Oberheide et al. (2002). The temperature non-migrating diurnal proxies at a single latitude, as a function of longitude λ, can be expressed by Eqn. 7 where T_1 and T_2 are expressions for tidal perturbations consisting of DE3 and DE2 at local times t_1 and t_2, respectively (see Eqns. 8 and 9). In this analysis, t_1 denotes a morning local time, t_2, an evening local time.

$$\Delta T(\lambda) = T_2(\lambda) - T_1(\lambda), \tag{7}$$

$$T_1(\lambda) = T_{DE3}\cos(\Omega t_1 - 4\lambda - \phi_{DE3}) + T_{DE2}\cos(\Omega t_1 - 3\lambda - \phi_{DE2}) + T_b, \tag{8}$$

$$T_2(\lambda) = T_{DE3}\cos(\Omega t_2 - 4\lambda - \phi_{DE3}) + T_{DE2}\cos(\Omega t_2 - 3\lambda - \phi_{DE2}) + T_b, \tag{9}$$

T_{DE3} and T_{DE2} denote the DE3 and DE2 temperature amplitudes, ϕ_{DE3} and ϕ_{DE2}, the DE3 and DE2 temperature phases. Ω is the Earth's rotation rate. T_b denotes a tidal bias term which vanishes in the local time difference. Eqn. 10 gives an analytical expression of the local time difference if only DE3 and DE2 contribute to the non-migrating diurnal proxy. Eqn. 11 is the corresponding expression for $\Sigma O/N_2$ where R_{DE3} and R_{DE2} denote the DE3 and DE2 $\Sigma O/N_2$ amplitudes, Φ_{DE3} and Φ_{DE2}, the DE3 and DE2 $\Sigma O/N_2$ phases.

$$\Delta T(\lambda) = 2T_{DE3}\cos\left(\Omega\frac{\Delta t}{2}\right)\cos\left(\Omega t_2 + \Omega\frac{\Delta t}{2} - 4\lambda - \phi_{DE3}\right) + 2T_{DE2}\cos\left(\Omega\frac{\Delta t}{2}\right)\cos\left(\Omega t_2 + \Omega\frac{\Delta t}{2} - 3\lambda - \phi_{DE2}\right), \tag{10}$$

$$\Delta R(\lambda) = 2R_{DE3}\cos\left(\Omega\frac{\Delta t}{2}\right)\cos\left(\Omega t_2 + \Omega\frac{\Delta t}{2} - 4\lambda - \Phi_{DE3}\right) + 2R_{DE2}\cos\left(\Omega\frac{\Delta t}{2}\right)\cos\left(\Omega t_2 + \Omega\frac{\Delta t}{2} - 3\lambda - \Phi_{DE2}\right), \tag{11}$$

The Δt terms account for the less than 12-hour local time differences and takes the value $\Delta t = t_2 - t_1 - 12$, which goes to zero for local time differences equal to 12 hours. The $\Sigma O/N_2$ tidal phases Φ_{DE3} and Φ_{DE2} are constrained by the prescribed phase differences at the latitude of interest (Eqns. 14 and 16). Θ_{DE3} and Θ_{DE2} are the temperature - $\Sigma O/N_2$ phase differences for DE3 and DE2 respectively. Here R_{DE3} and R_{DE2} are taken to equal their respective temperature amplitudes (Eqns. 13 and 15).

$$T_{res}^2 + R_{res}^2 = [T_{obs}(\lambda) - \Delta T(\lambda)]^2 + [R_{obs}(\lambda) - \Delta R(\lambda)]^2, \tag{12}$$

$$R_{DE3} = T_{DE3}\,, \tag{13}$$

$$\Phi_{DE3} = \phi_{DE3} - \Theta_{DE3}\ , \tag{14}$$

$$R_{DE2} = T_{DE2}\ , \tag{15}$$

$$\Phi_{DE2} = \phi_{DE2} - \Theta_{DE2}\ , \tag{16}$$

In October, we require that $T_{DE3} \geq 3T_{DE2}$ to ensure that DE3 is much higher in amplitude than DE2. This constraint is justified for this season because DE3 has consistently been identified as the dominant non-migrating diurnal component around September equinox (Forbes et al., 2006; Nischal et al., 2019). In order to deduce the tides, the normalized non-migrating diurnal proxies for temperature and $\Sigma O/N_2$, T_{obs} and R_{obs}, are simultaneously fitted to Eqns. 10 and 11. A least-squares scheme determines the combination of temperature tidal parameters T_{DE3}, T_{DE2}, ϕ_{DE3}, and ϕ_{DE2} that yields the lowest total squared residual $T_{res}^2 + R_{res}^2$ (Eqn. 12). We have implemented a pattern search optimization approach (Lewis et al., 2000) to efficiently determine a solution. The five best combinations of tidal parameters are determined from a 25 ×25 ×25 ×25 parameter grid and serve as initial guesses. For each initial guess, the residual value is then compared to those at each of its neighboring grid points after the parameter grid resolution is halved. If one of the neighboring grid points yields a lower total squared residual, then the center moves to that point. If the center is the best guess, then the parameter grid resolution is further halved. This process proceeds until there have been 4 reductions. The deduced tidal parameters are taken from best result out of the five pattern searches starting from the initial guesses. The retrieved amplitudes are then converted back to geophysical units using the maximum perturbations M_T and M_R.

4) Results

4.1 TIE-GCM Sensitivity Analyses

Testing our approach on the TIE-GCM-simulated GOLD dataset, consisting of the effective neutral temperature and vertical column density ratio of O to N_2 (described in Section 2), allows us to examine its reliability when applied to a dataset in which the true tides are known. This dataset contains a realistic tidal spectrum and is sampled in the observational geometry of GOLD. Two test cases are considered: October and January during solar minimum conditions. For both, we deduce DE3 and DE2 between -21.25º to 21.25º latitude. We restrict our analysis to this latitude range as it is where DE3 and DE2 have their largest amplitudes (Figures 2 and 3). Robustness of our algorithm to noise is tested using runs at 5 linearly increasing levels of random noise where the maximum noise magnitude for temperature is 60 Kelvins and 0.08 (~15%) for $\Sigma O/N_2$. We performed 10 simulations at each noise level and compare the average result to the truth to reduce random effects in the amplitude and phase errors.

During October, DE3 is the most dominant non-migrating tide (Figure 2). Shown in Figure 4a is the percent error in the temperature amplitude retrieval for DE3 as a function of latitude and random noise magnitude. Figures 4b shows the absolute error (in units of hours of universal time) of the phase retrieval for DE3. The $\Sigma O/N_2$ results are similar and are thus not shown. The errors in the deduced DE2 tide are not shown because the DE2 amplitude is small during October. The DE3 phases (Figure 4b) are retrieved very accurately even in the case of maximum random noise. The error in the deduced DE3 amplitude (Figure 4a) strongly depends on random noise amplitude and latitude. For the lowest noise amplitudes, the error is negligible. For the case of maximum noise amplitude, the DE3 temperature amplitude was overestimated by about

60% at around 21.25º N, but elsewhere the error is no more than about 40%. To assess the assumption that only two tides are present, we applied our approach to a modified dataset where we remove the terdiurnal tide and all components in the non-migrating diurnal spectrum except for DE3 and DE2. This filtering removes the tidal aliasing caused by components assumed to be zero and removes any bias in the zonal mean caused by a partially viewed component such as DO, for example. It was found that the errors in deduced tidal parameters do not change appreciably (not shown). This suggests that tidal aliasing does not play a major role and that the errors present in Figure 4 are primarily due to random noise and the restriction in longitude.

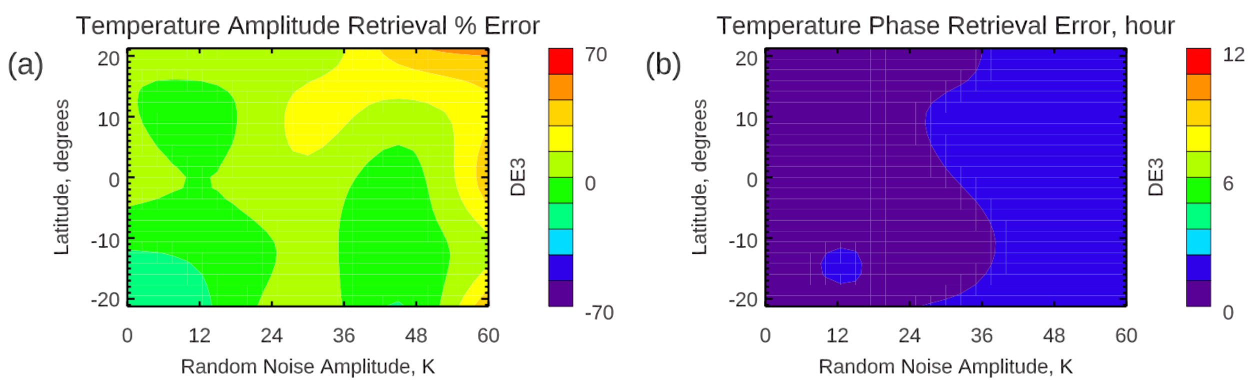

Figure 4. *Retrieval errors as a function of latitude and random noise amplitude for DE3 temperature tidal amplitudes (a) and phases (b) when applying our approach to a simulated GOLD dataset for October and solar minimum conditions.*

Figure 5 is the same as Figure 4 but for January. The errors in the deduced DE2 are included since, along with DE3, it is the leading non-migrating diurnal tide (Figure 3). Figures 5a and 5c show the percent error in the deduced temperature amplitude for DE3 and DE2 respectively. Aside from a few results around 21.25º N for higher noise amplitudes, the amplitude retrieval errors are small for both DE3 and DE2. Phase retrieval error as shown by Figures 5b and 5d is negligible for both DE3 and DE2, always less than 4 hours. As was done for October, we applied our approach to a modified dataset where only DE3 and DE2 remain. Similarly, it was found that the errors in the retrieved tidal parameters do not change appreciably. This leads to the same conclusion that random noise and the restriction in longitude play a much larger role than aliasing of tides assumed to be absent.

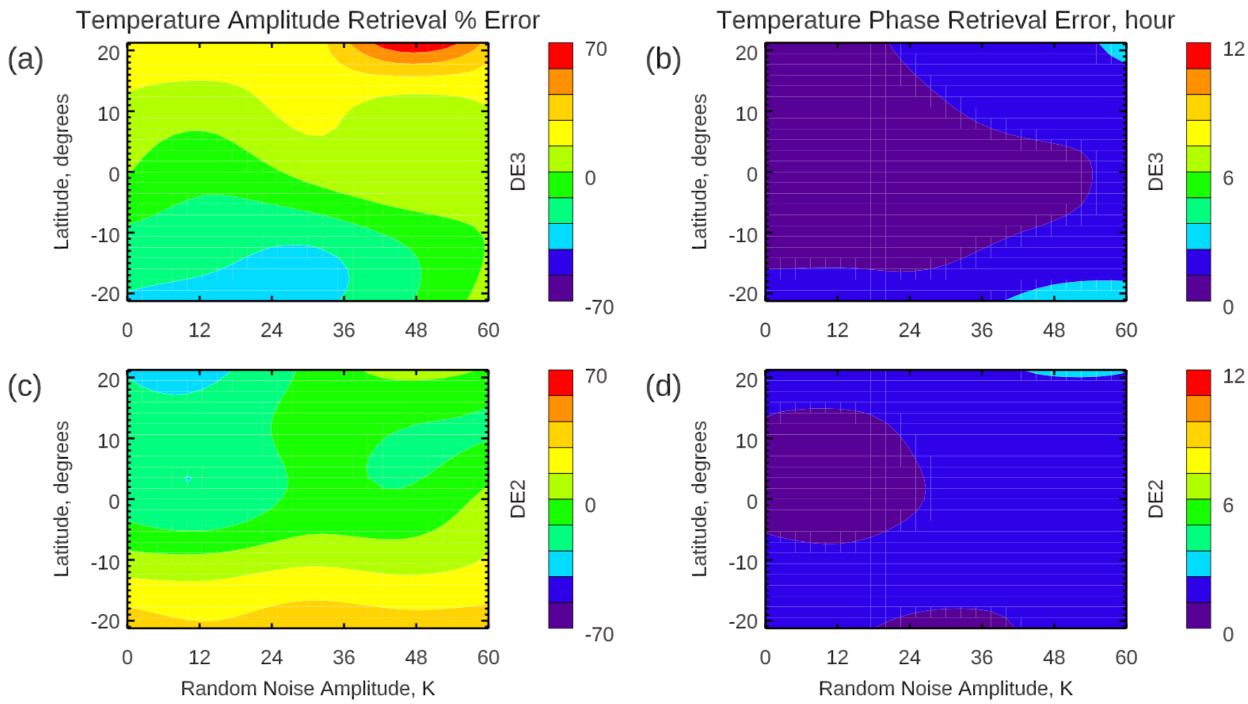

__Figure 5.__ Same as Figure 4, but for January and the errors in the retrieved DE2 tidal parameters are also shown.

4.2 Application to the GOLD Dataset

In this subsection we discuss application of our approach (discussed in Section 3) to GOLD observations from two weeks during different seasons: 21-27 October 2018 and 8-14 January

2020. These fitting periods were selected to be representative of times when non-migrating tides are strong and somewhat different and to avoid times when rapid changes occur, e.g., during a sudden stratospheric warming or geomagnetic storm. Our analysis is conducted between -25º to 25º latitude like the previous section. A description of our GOLD data analysis method is provided here. We initially analyze the data in the irregularly spaced latitude-longitude spatial grid provided in the GOLD data products. While this would not be justified at mid to high latitudes, there is only a negligible change in latitude across a row of pixels reported on the disk within this latitude range. Non-migrating tides are known to undergo day-to-day variability (Pedetalla et al., 2016; Li et al., 2015). To lessen the impact of short-term tidal variability on our fits, the value at each disk pixel (longitude, latitude) and scan (universal time) in our analysis represents the mean over the respective weeks in October 2018 and January 2020. About 68 GOLD dayside disk scans are performed at about the same universal times each day during the respective time periods. It is assumed that the tidal amplitudes and phases are time-invariant during the fitting period. This assumption is common to any tidal diagnostic technique which analyzes data over a fitting period spanning multiple days, e.g., Zhang et al., (2006). GOLD disk neutral temperature responds episodically to variations in geomagnetic and solar activity (not shown) while O/N_2 exhibits response to geomagnetic activity (Cai et al., 2020). Therefore, we disregard measurements taken on days with sufficient geomagnetic or solar activity. Our geomagnetic activity threshold is Kp > 4 and our solar activity threshold is a F10.7cm index more than 2.5 standard deviations higher than the mean F10.7cm index over a window equal to the fitting period +/- 7 days. Data for a given pixel/scan that are 2 standard deviations from the median value are disregarded in the mean value. Also, we disregard the edge rows of pixels around the equator where data quality may be lower (due to reduced sensitivity of the detector near the end of the entrance slit). The standard deviation for the 7-day means corresponding to a given pixel/scan is on average about 50 K for temperature and 6% relative to the zonal mean for $\Sigma O/N_2$ at the latitudes/SZA analyzed. Additionally, we found it necessary to remove linear trends with longitude from the non-migrating diurnal proxies (especially $\Sigma O/N_2$) at some latitudes. This linear detrending makes the salient wave signal more apparent. One may consider that the linear trends with longitude are the actual tides (which must have zonal wavelengths larger than the GOLD field-of-regard, i.e., zonal wavenumber 1 or 2), and the residuals reflect random noise. But this is unlikely since analysis of slightly offset fitting periods or the same season in different years yields similar $\Sigma O/N_2$ morphology after the linear trends are removed (not shown). Before performing the least squares fit to the tidal perturbation equations, we interpolate the normalized longitudinal perturbations to an evenly spaced longitude grid so that each sector of longitude is equally weighted in the fit. The non-migrating diurnal proxies are also smoothed in the longitude dimension. We estimate the resultant damping of the dominant tidal amplitudes(s) is on the order of 5%. In what follows, we present results for each time period.

GOLD mission science operations began in October 2018 and hence observations taken during this time are not affected by detector burn-in or grating yaw mechanism (GYM) shifts characteristic of the GOLD Mission over time (McClintock et al., 2020a; McClintock et al., 2020b). Both TIE-GCM simulations (see Figure 2) and SABER observations of MLT temperature (Forbes et al, 2006) indicate that DE3 is the dominant tidal component at around September equinox. DE2 is the secondary tide in our analysis during this time because of its similar modal structure to that of DE3. In Figure 6, we compare global maps of the dusk – dawn difference (non-migrating diurnal proxy) and the retrieved tides (DE3 + DE2) for temperature (K) and $\Sigma O/N_2$ (% relative to the zonal mean at each latitude). Figures 6a and Figure 6b respectively indicate peak-to-peak perturbations of about 32 K and 7%. The latitudinal structure is not symmetric, and the phase rapidly changes with latitude especially in temperature. It is noteworthy that both the temperature and the $\Sigma O/N_2$ dusk and dawn differences exhibit these features. This similarity may be explained by a combination of (1) similar tidal dynamics and (2) instrument or processing artifacts. It is not surprising that the northern hemisphere and southern hemisphere are not coherent since there are clear hemispheric biases in the GOLD disk neutral temperature and $\Sigma O/N_2$ measurements (not shown) caused by varying instrument characteristics along the slit that are not currently removed in the processing of FUV radiances (McClintock et al., 2020b). Additionally, the relatively high uncertainty in the retrieved disk neutral temperature at high SZA analyzed leads to the noisy dusk – dawn differences in Figure 6a, perhaps best exemplified by the unphysical change in temperature north of (60º W, 15º N). In general, the retrieved tides generally reproduce the large-scale morphology of the dusk – dawn differences (compare Figure 6a to 6b and 6c to 6d). It does not do so when the phase difference between temperature and $\Sigma O/N_2$ do not remotely match the prescribed phase differences provided by TIE-GCM. Figures 7 and 8 respectively show the retrieved amplitudes and phases as functions of latitude. We only show latitudes where the correlation coefficient between the non-migrating diurnal proxy and retrieved tides is greater than 0.75 for both temperature and $\Sigma O/N_2$. The error bars represent the root mean square deviation of the least squares fit at each latitude and indicate the degree of uncertainty. Figure 7a shows that the DE3 temperature amplitude is mostly above 10 K which is greater than that from TIE-GCM (Figure 2a). The DE3 $\Sigma O/N_2$ amplitudes shown in Figure 7b are markedly higher in the southern hemisphere than in the northern hemisphere. The amplitude in the southern hemisphere is greater than that from TIE-GCM (Figure 2b). Results for DE2 amplitudes (Figures 7c and 7d) are similar but much lower in amplitude. The results in Figure 7 suggest the DE3 and DE2 amplitudes required to generate the perturbations in Figures 6a and 6b and provide the first estimates of non-migrating diurnal tidal amplitudes in middle thermosphere temperature. Phases as a function of latitude are shown in Figure 8 in units of universal time of maximum at 0º longitude. All the retrieved phases for a given component and parameter appear to be within about 4 hours. This suggests that we are seeing the same wave at these latitudes while the tides at other latitudes are perhaps obscured by instrument artifacts or limitations associated with using GOLD disk neutral temperature at high SZA.

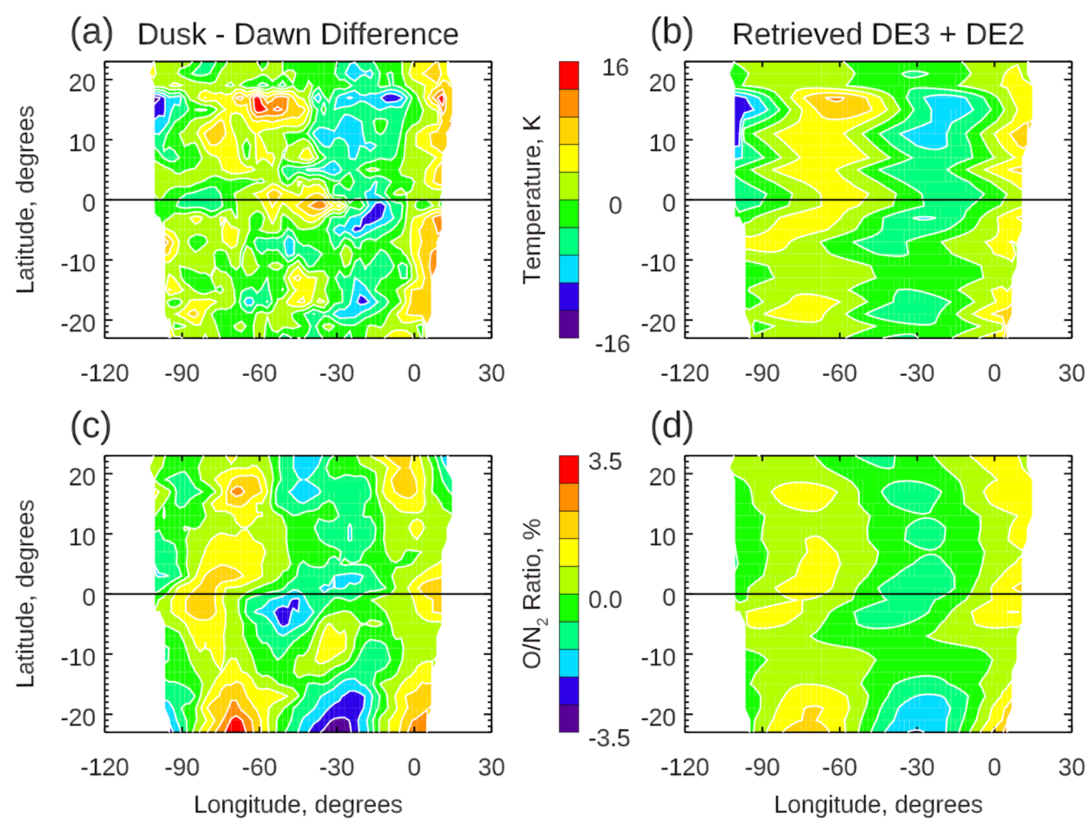

Figure 6. *Global maps of the dusk – dawn differences and retrieved tides DE3 + DE2 in neutral temperature, (a) and (b), and column O/N_2 ratio, (c) and (d), from GOLD data in October 2018.*

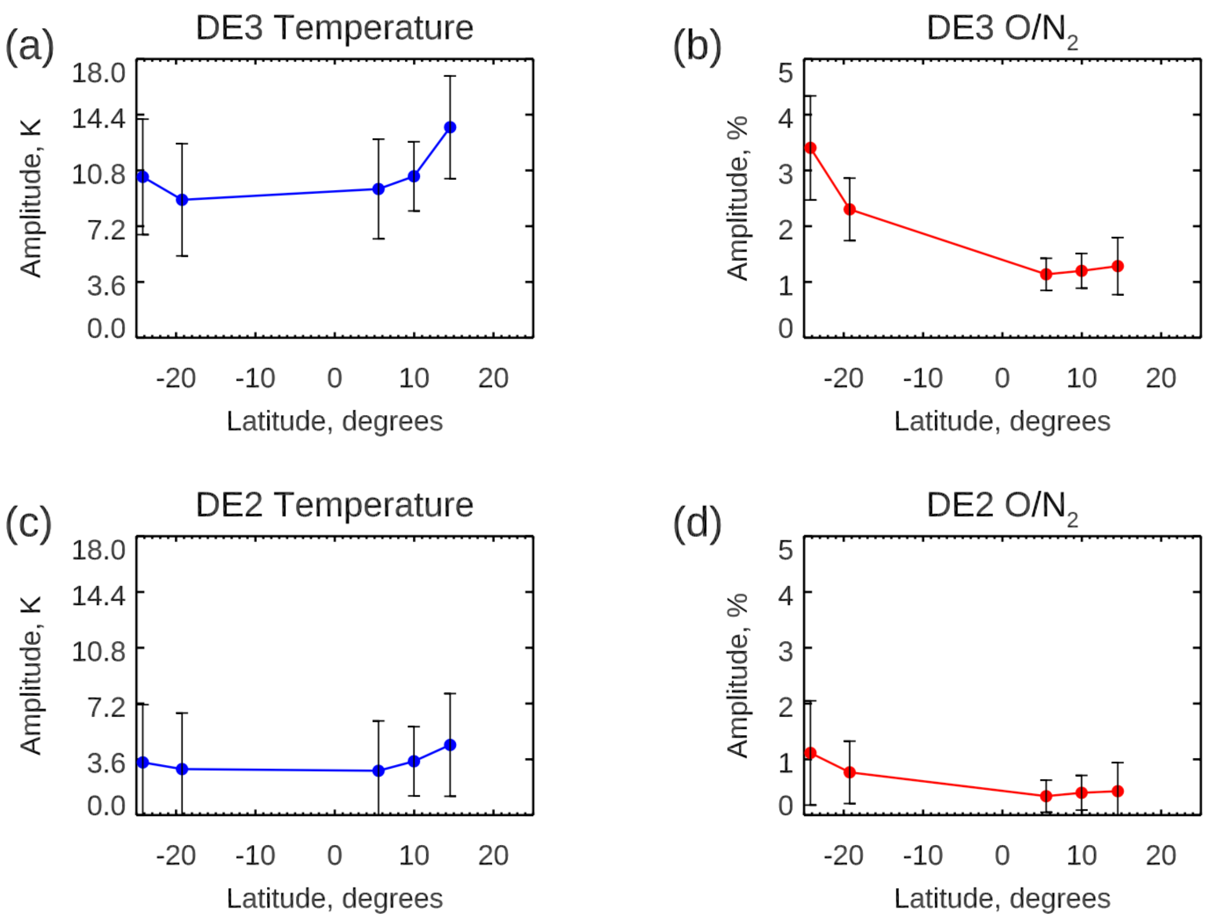

Figure 7. *Retrieved amplitudes from GOLD data during October 2018 as a function of latitude for DE3, (a) and (b), and DE2, (c) and (d). Errors bars reflect the root mean square deviation of the least squares fit at each latitude. Only latitudes where the least squares fit in both temperature and O/N*$_2$ *yields a correlation coefficient greater than 0.75 are shown.*

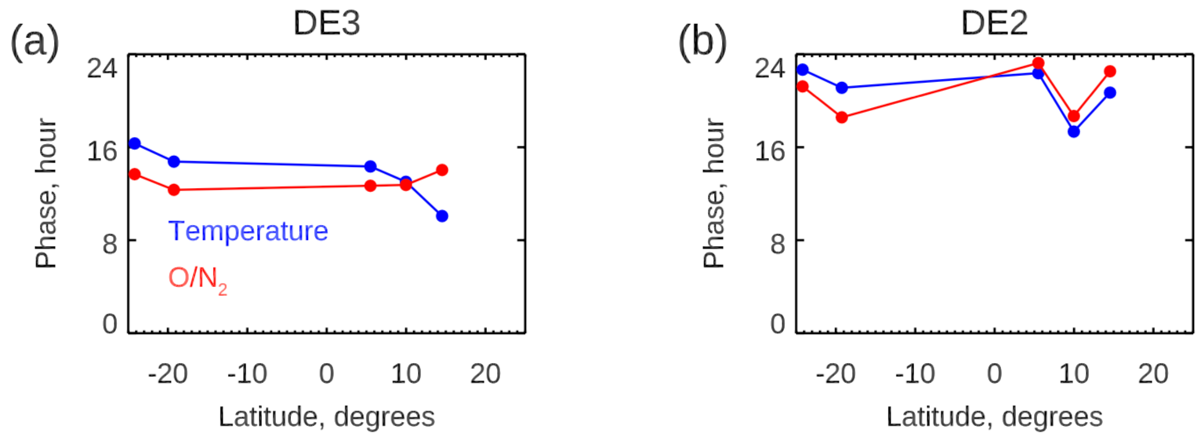

Figure 8. *Retrieved phases (universal time of maximum at 0° longitude) from GOLD data during October 2018 as a function of latitude for DE3 (a) and DE2 (b). Temperature is shown in blue, O/*N_2 *in red. Only latitudes where the least squares fit in both temperature and O/*N_2 *yields a correlation coefficient greater than 0.75 are shown.*

TIE-GCM (Figure 3) indicates that DE3 and DE2 are the leading components in the non-migrating diurnal spectrum around January solstice. Forbes et al. [2008] analyzed TIMED/SABER temperatures from 2003-2005 and showed that DE2 was the dominant non-migrating diurnal tide at the equator and at 116 km altitude around January solstice, with DE3 being minor. Informed by both modeling and observations, we deduce DE3 and DE2 during January 2020. Figures 9, 10, and 11 are the same as Figures 6, 7, and 8 but when we apply our approach to GOLD data analyzed over 8-14 January 2020. The dusk – dawn differences (Figures 9a and 9c) respectively have peak-to-peak perturbations of about 42 K and about 11%. Figure 9b and 9d reproduce the large-scale structure present in Figures 9a and 9c respectively. Figure 9a, like its October counterpart (Figure 6a), exhibits seemingly random fluctuations as well as a lack of latitude symmetry. The same reasons discussed above for October 2018 likely explain these features. Figure 9c shows that for $\Sigma O/N_2$ there is a coherent structure in the non-migrating diurnal tide with zonal wavelength approximately equal to 100º of longitude between -10º S and 25º N. This suggests that a superposition of DE3 and DE2 are responsible for generating the signature. Figures 10a and 10b indicate that both the DE3 and DE2 temperature amplitudes are on the order of 10 K barring the outlier results at -25º S and -25º N which have large error bars. Figure 10b shows that the DE3 $\Sigma O/N_2$ amplitude is highest around the equator (~ 4.8%), while Figure 10d shows DE2 $\Sigma O/N_2$ amplitude is highest in the northern hemisphere. The DE2 phases (Figure 11b) deviate no more than about 4 hours from 0:00 except at -1º S, while the DE3 phases vary more with latitude. This suggests that the DE3 retrieval is perhaps more impacted by instrument artifacts and limitations associated with using GOLD disk neutral temperature at high SZA while the DE2 seen is a single coherent wave.

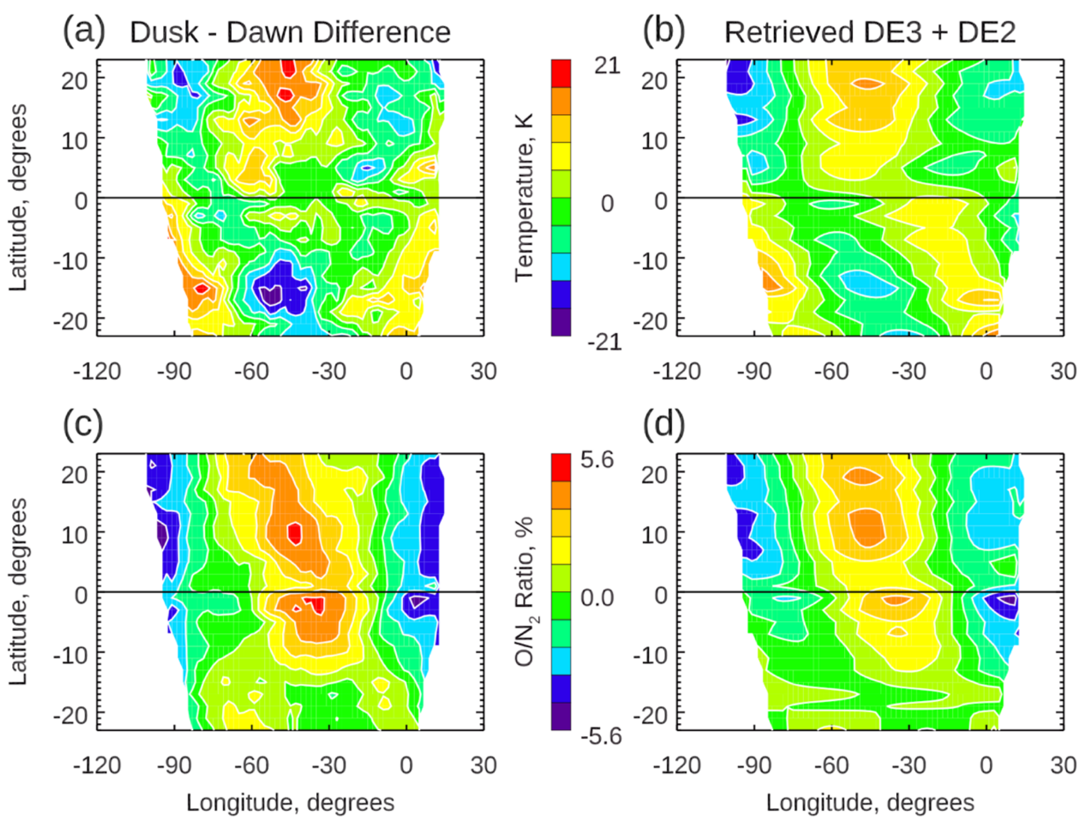

Figure 9. *Same as Figure 6 but for January 2020.*

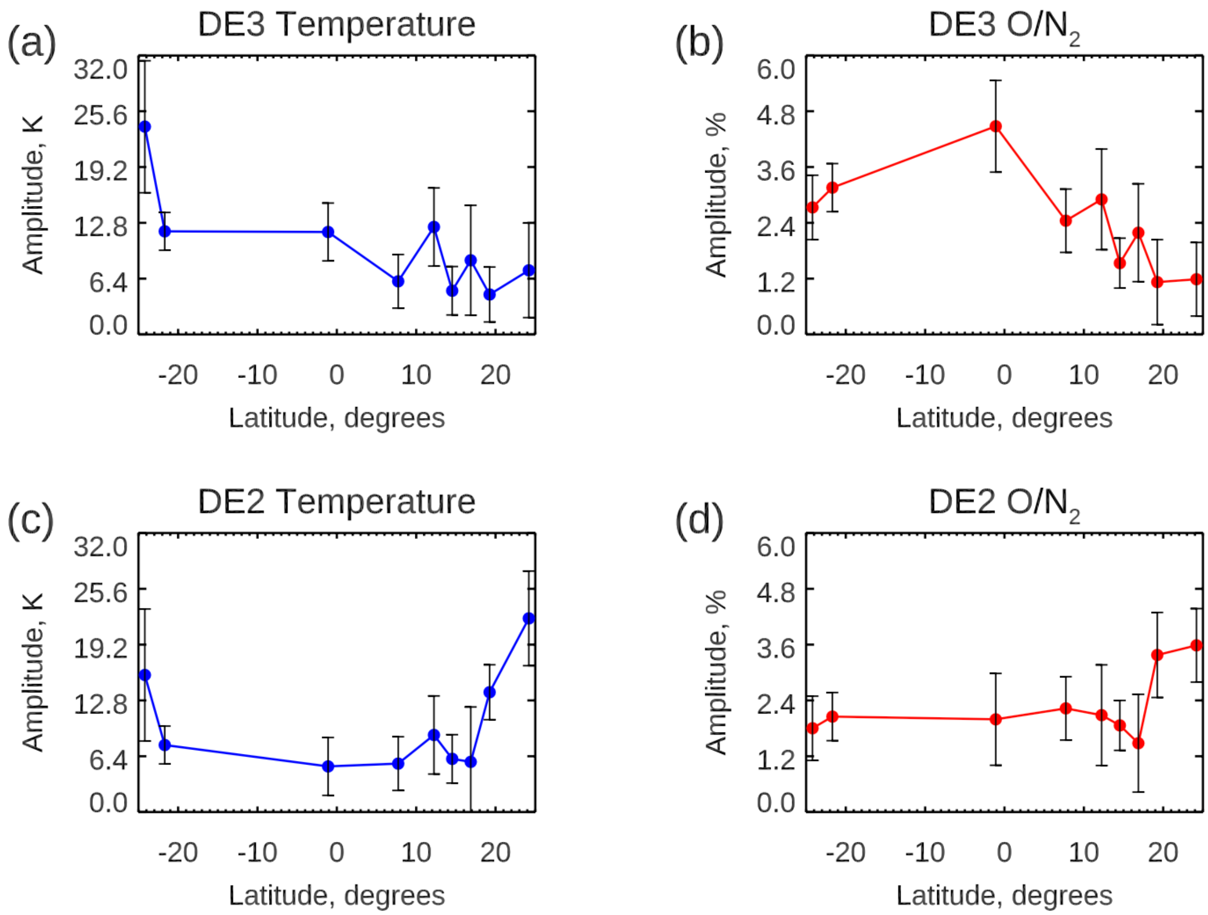

Figure 10. *Same as Figure 7 but for January 2020.*

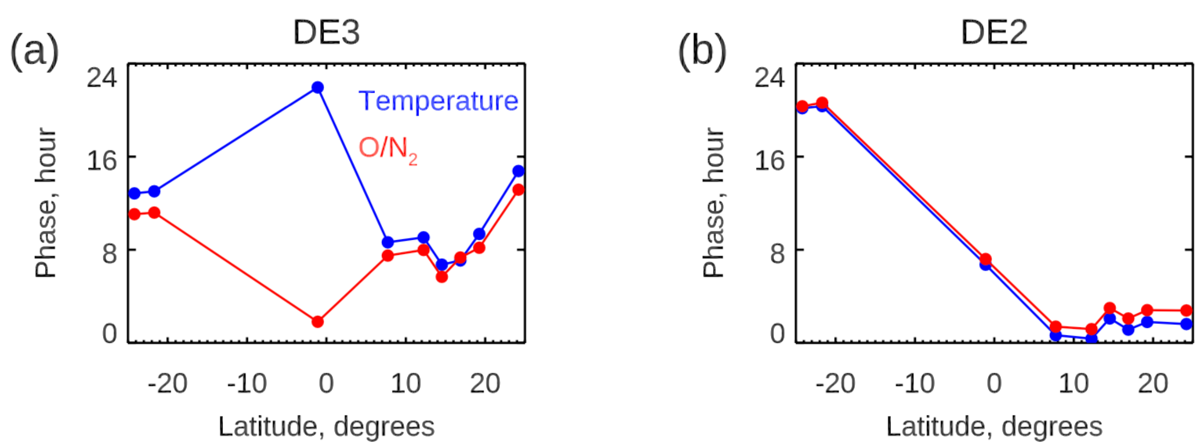

Figure 11. Same as Figure 8 but for January 2020.

4.3 Assessing the Impact of Ionospheric Contamination

O+ radiative recombination by the equatorial arcs has the potential to impact the global structure of the $\Sigma O/N_2$ dusk – dawn differences. Previous studies (e.g., Kil et al., (2013) and references therein) have shown that investigations of non-migrating tides in $\Sigma O/N_2$ retrieved from far ultraviolet dayglow are impacted by O^+ radiative recombination in the ionosphere, concentrated around the equatorial ionization anomaly (EIA), which emits at the same wavelength, 135.6 nm, used in the $\Sigma O/N_2$ retrieval. Kil et al. (2013) concluded that the longitudinal wave patterns in GUVI $\Sigma O/N_2$ near 15:00 LT mostly reflect the ionosphere 135.6 nm emissions. The tidal variations in the O^+ radiative recombination likely correlate with those in F-region plasma density which are driven by E-region dynamo modulation by tidal winds (England et al., 2006; Immel et al., 2006). In general, the $\Sigma O/N_2$ tidal signatures near the EIA may be produced by a superposition of the thermospheric tides and the ionospheric contamination, which should both have the same wavenumber structure but are out of phase. It is expected that $\Sigma O/N_2$ near the morning terminator is less impacted by the ionosphere (since nighttime recombination depresses the O+ density). In the following, we assess the potential impact of ionospheric contamination on the $\Sigma O/N_2$ non-migrating diurnal proxies used in our approach. GOLD has the unique advantage of measuring post-sunset 135.6 nm emissions of the ionosphere in the same sector of the Earth over which $\Sigma O/N_2$ is retrieved during daytime (Eastes et al., 2019). We use version 04 GOLD night scans, exclusively channel B, to construct a map of post-sunset 135.6 nm emissions by averaging into a local time bin extending from 19:00-22:00 LT. These maps serve as a proxy for the ionospheric contribution to 135.6 nm emissions around dusk used in the $\Sigma O/N_2$ retrieval. The maps are constructed using data from 21-27 October 2018 and 8-14 January 2020. When analyzed in the same fashion, the dusk – dawn difference of the ratio of the 135.6 nm and LBH band (1356/LBH) intensities correlate extremely well (not shown) with those of $\Sigma O/N_2$ (shown in Figures 6c and 9c) since $\Sigma O/N_2$ is derived from 1356/LBH. We can therefore assess the potential impact of ionospheric contamination on our approach by first removing the post-sunset 135.6 nm emissions from the dusk 135.6 nm emissions used in the retrieval of $\Sigma O/N_2$ and then recomputing the 1356/LBH ratio. Figures 12a and 12b compare 1356/LBH brightness ratios before and after the post-sunset 135.6 nm emissions are removed for the period during October 2018. Note that there is a gap of longitudinal coverage on the western side of the disk because GOLD does not perform night scans in the entire region over which GOLD performs day scans. Figure 12c shows the difference of the 1356/LBH before and after treating for ionospheric contamination. This difference resembles the map of post-sunset 135.6 (Figure 12d) used in the removal. The geomagnetic equator is indicated as a dashed line in Figure 12d, and the brightest post-sunset 135.6 nm emissions clearly follow the equatorial arcs and exhibit longitudinal asymmetry, especially in the southern hemisphere. By looking at Figure 12d and by comparing Figures 12a and 12b, we can conclude that while the ionospheric contamination does not seem to global structure of the 1356/LBH pattern in October 2018, it does appreciably affect the longitude asymmetry. Therefore, ionospheric contamination does not affect the zonal wavenumber or phase and likely thus does not fundamentally change the retrieved tides. Figure 13 is the same as Figure 12 but for January 2020. Note that the post-sunset 135.6 nm emissions (Figure 13d) are dimmer during this time and the resulting difference between the 1356/LBH brightness ratios before and after treating ionospheric contamination (Figure 13c) is smaller. It is evident that ionospheric contamination has a seasonal dependence such that our results in October 2018 are more likely to be impacted by ionospheric contamination. It is conceivable to produce a revised GOLD $\Sigma O/N_2$ product where the post-sunset 135.6 nm emissions are removed from the retrieval input near dusk, but this is beyond the scope of the current work. From the above analysis, we expect the ionospheric signature in GOLD $\Sigma O/N_2$ non-migrating tides to be minimal due to the pronounced dip in the magnetic equator with respect to the geographic equator across the Earth in GOLD's field-of-regard which would tend to smooth out any ionospheric signature in the non-migrating tides.

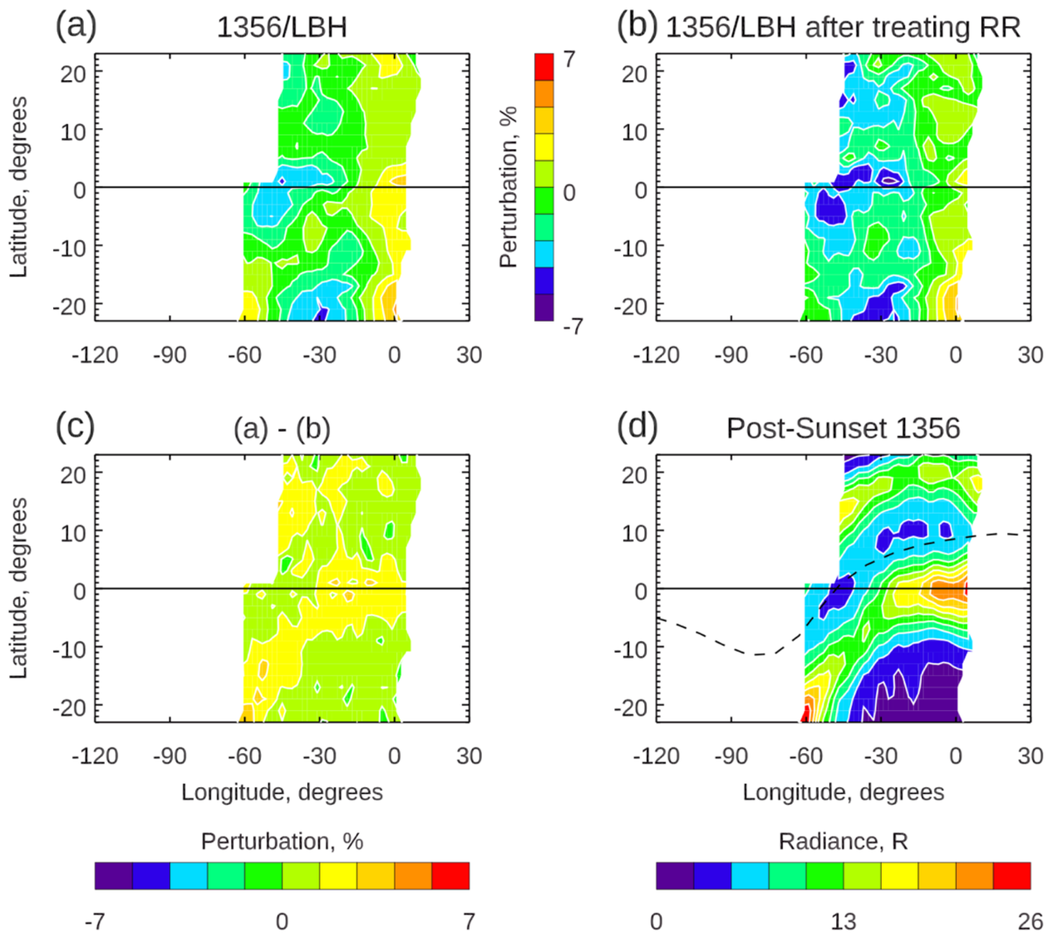

Figure 12. *Dusk-dawn differences of 1356/LBH intensity ratios before (a) and after (b) O+ RR is removed from the dusk 1356 radiances. Presented as perturbations from the zonal mean of the 1356/LBH ratio. (c) shows the difference of (a) and (b). The global map (d) of post-sunset 1356 used in the O+ RR treatment. The dashed line indicates the geomagnetic equator.*

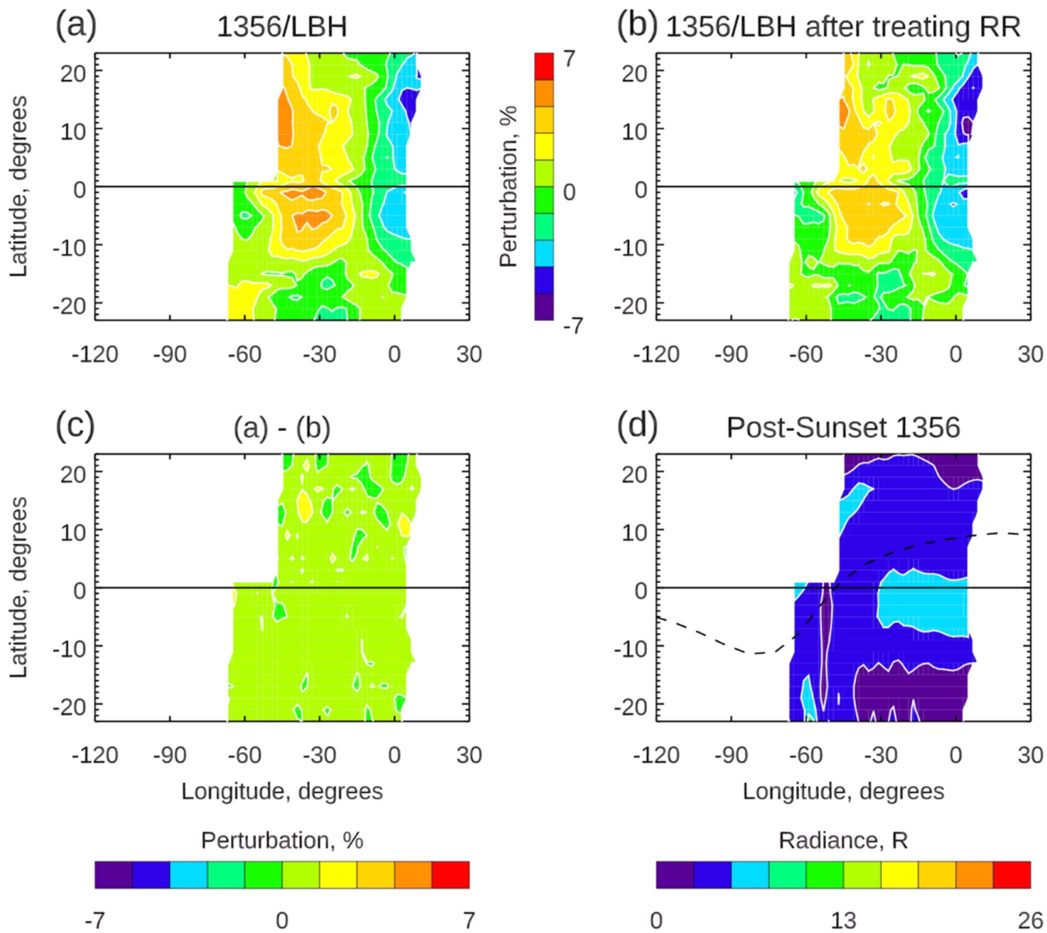

Figure 13. *Same as Figure 12 but for January 2020.*

5) Summary and Conclusions

We have presented a novel approach to deducing non-migrating diurnal tides in the middle thermosphere using observations of far ultraviolet airglow from geostationary orbit. The incomplete longitudinal/local time sampling as well as the nature of the effective temperature measurement preclude a full tidal decomposition. Our unique approach derives the leading non-migrating diurnal tides from simultaneous measurements of temperature and composition

($\Sigma O/N_2$) by taking dusk – dawn differences and fitting two specified tides, DE3 and DE2, for example, while constraining temperature-composition phase relationships using TIE-GCM.

In Section 4.1, we tested our approach on a simulated GOLD dataset where the amplitudes and phases are known using TIE-GCM. The noise sensitivity analysis discussed in Section 4.1 suggests that even in the case of significant random noise, our approach reliably retrieves the phases of the dominant tides during both October and January. Results for January highlight our approach's ability to deduce two tides simultaneously. It was found that the presence of tides other than those being deduced does not appreciably change the results indicating that the primary sources of error are the restriction in longitude and the presence of substantial random noise. The error in the retrieved amplitude can be as large as 50% at some latitudes. Nonetheless, even estimates with ~ 50% amplitude retrieval errors provide much needed constraints on temperature tides in the middle thermosphere. We speculate that our approach would benefit greatly from a constellation of GOLD-like instruments providing complete longitudinal coverage.

We have presented a preliminary application of our approach to GOLD data and revealed non-migrating diurnal features during October 2018 and January 2020. There are substantial peak-to-peak variations in both temperature and $\Sigma O/N_2$ during these times as large as 42 K and 11% respectively. The retrieved amplitudes and phases suggest that a superposition of DE3 and DE2 explains the non-migrating diurnal variations during October 2018 and January 2020. We estimate the DE3 and DE2 amplitudes required to generate the perturbations which mostly exceed the respective TIE-GCM amplitudes. During both October 2018 and January 2020, the non-migrating diurnal proxies show unexpected rapidly changing phases with latitude, while those for temperature are exceptionally noisy because of the relatively high uncertainty in disk neutral temperature at high SZA. Consequently, the retrieved amplitudes and phases do not strongly resemble the coherent amplitude and phase structures from TIE-GCM. We speculate that this could arise as the result of a combination of instrument and processing artifacts, limitations associated with relatively high uncertainty in disk neutral temperature at high SZA, and ionospheric contamination. An assessment using GOLD night scans (Section 4.4) suggests that ionospheric contamination has an appreciable effect on the non-migrating diurnal tide seen in October 2018, but it does not fully explain the discrepancies with TIE-GCM simulation. It was found that the ionospheric contamination is much weaker in January 2020 and therefore varies with season. The ionospheric contribution to the tidal variations in $\Sigma O/N_2$ has not yet been fully characterized. Interpretation of the amplitude and phase structures can be enhanced by additional observational efforts aimed at identifying and removing ionospheric contribution from the retrieval of $\Sigma O/N_2$ which will be the topic of a future work. Nevertheless, in this work, we have presented valuable observations of non-migrating diurnal tides in the middle thermosphere temperature and composition using GOLD, the first of its kind from an observational platform in geostationary orbit.

Data Availability Statement

GOLD data are available from the GOLD Science Data Center (http://gold.cs.ucf.edu/search/) and the NASA Space Physics Data Facility (https://spdf.gsfc.nasa.gov). The TIE-GCM tidal parameters and contribution function used in this work are available for peer-review purposes at https://figshare.com/s/1e29f99114a466f4dc08?file=27913752 (this will later be moved to the Virginia Tech Library permanent repository and assigned a DOI).

Acknowledgements

This research was supported by NASA contract 80GSFC18C0061. The authors would like to thank J. Correira (Computational Physics, Inc.) for reprocessing GOLD ON2 files used in the preparation of this work.

References

Cai, X., Burns, A. G., Wang, W., Qian, L., Solomon, S. C., Eastes, R. W., et al. (2020). The two-dimensional evolution of thermospheric $\sum O/N_2$ response to weak geomagnetic activity during solar minimum observed by GOLD. *Geophysical Research Letters*, 47, e2020GL088838. https://doi.org/10.1029/2020GL088838.

Cai, X., Burns, A. G., Wang, W., Qian, L., Solomon, S. C., Eastes, R. W., et al. (2021). Investigation of a neutral 'tongue' observed by GOLD during the geomagnetic storm on May 11, 2019. *Journal of Geophysical Research: Space Physics*, 126, e2020JA028817. https://doi.org/10.1029/2020JA028817.

Correira, J., Evans, J. S., Krywonos, A., Lumpe, J. D., Veibell, V., McClintock, W. E., & Eastes, R. W. (2020). Thermospheric composition and solar EUV flux from the Global-scale Observations of the Limb and Disk (GOLD) mission. *Earth and Space Science Open Archive*, *36*. https://doi.org/10.1002/essoar.10501920.1.

Cui, J., R. V. Yelle, T. Li, D. S. Snowden, and I. C. F. Müller-Wodarg (2014), Density waves in Titan's upper atmosphere, *J. Geophys. Res. Space Physics*, 119, 490–518, doi:10.1002/2013JA019113.

Eastes, R. W., McClintock, W. E., Burns, A. G., Anderson, D. N., Andersson, L., Codrescu, M., et al. (2017). The Global-Scale Observations of the Limb and Disk (GOLD) Mission. *Space Science Reviews*, 212(1-2), 383–408. https://doi.org/10.1007/s11214-017-0392-2.

Eastes, R. W., McClintock, W. E., Burns, A. G., Anderson, D. N., Andersson, L., Aryal, S., et al. (2020). Initial observations by the GOLD mission. *Journal of Geophysical Research: Space Physics*, *125*, e2020JA027823. https://doi.org/10.1029/2020JA027823.

Eastes, R. W., Solomon, S. C., Daniell, R. E., Anderson, D. N., Burns, A. G., England, S. L., et al. (2019). Global-scale observations of the equatorial ionization anomaly. *Geophysical Research Letters, 46*, 9318–9326. https://doi.org/10.1029/2019GL084199.

England, S. L. (2012), A review of the effects of non-migrating atmospheric tides on the Earth's low-latitude ionosphere, *Space Sci. Rev.*, 168, 211–236, doi:10.1007/s112140119842-4.

England, S. L., Immel, T. J., Huba, D., Hagan, M. E., Maute, A., & DeMajistre, R. (2010). Modeling of multiple effects of atmospheric tides on the ionosphere: An examination of possible coupling mechanisms responsible for the longitudinal structure of the equatorial ionosphere. *Journal of Geophysical Research*, 115, A05308. https://doi.org/10.1029/2009JA014894.

England, S. L., S. Maus, T. J. Immel, and S. B. Mende (2006), Longitudinal variation of the E-region electric fields caused by atmospheric tides, *Geophys. Res. Lett.*, 33, L21105, doi:10.1029/2006GL027465.

Forbes, J. M., J. Russell, S. Miyahara, X. Zhang, S. Palo, M. Mlynczak, C. J. Mertens, and M. E. Hagan (2006), Troposphere-thermosphere tidal coupling as measured by the SABER instrument on TIMED during July–September 2002, *J. Geophys. Res.*, 111, A10S06, doi:10.1029/2005JA011492.

Forbes, J. M., X. Zhang, S. Palo, J. Russell, C. J. Mertens, and M. Mlynczak (2008), Tidal variability in the ionospheric dynamo region, *J. Geophys. Res.*, 113, A02310, doi:10.1029/2007JA012737.

Forbes, J. M., X. Zhang, E. R. Talaat, and W. Ward (2003), Nonmigrating diurnal tides in the thermosphere, *J. Geophys. Res.*, 108(A1), 1033, doi:10.1029/2002JA009262.

García-Comas, M., F. González-Galindo, B. Funke, A. Gardini, A. Jurado-Navarro, M. López-Puertas, and W. E. Ward (2016), MIPAS observations of longitudinal oscillations in the mesosphere and the lower thermosphere: Part 1. Climatology of odd-parity daily frequency modes. *Atmos. Chem. Phys. Discuss.* doi:10.5194/acp-2015-1065.

Gasperini, F., J. M. Forbes, E. N. Doornbos, and S. L. Bruinsma (2015), Wave coupling between the lower and middle thermosphere as viewed from TIMED and GOCE, *J. Geophys. Res. Space Physics*, 120, 5788–5804, doi:10.1002/2015JA021300.

Hagan, M. E., and J. M. Forbes (2002), Migrating and nonmigrating diurnal tides in the middle and upper atmosphere excited by tropospheric latent heat release, *J. Geophys. Res.*, 107(D24), 4754, doi:10.1029/2001JD001236.

Hagan, M. E., A. Maute, R. G. Roble, A. D. Richmond, T. J. Immel, and S. L. England (2007), Connections between deep tropical clouds and the Earth's ionosphere, *Geophys. Res. Lett.*, 34, L20109, doi:10.1029/2007GL030142.

Häusler, K., and H. Lühr (2009), Nonmigrating tidal signals in the upper thermospheric zonal wind at equatorial latitudes as observed by CHAMP, *Ann. Geophys.*, 27(7), 2643–2652, doi:10.5194/angeo-27-2643-2009.

He, M., L. Liu, W. Wan, J. Lei, and B. Zhao (2010), Longitudinal modulation of the O/N_2 column density retrieved from TIMED/GUVI measurement, *Geophys. Res. Lett.*, 37, L20108, doi:10.1029/2010GL045105.

Immel, T. J., E. Sagawa, S. L. England, S. B. Henderson, M. E. Hagan, S. B. Mende, H. U. Frey, C. M. Swenson, and L. J. Paxton (2006), Control of equatorial ionospheric morphology by atmospheric tides, *Geophys. Res. Lett.*, 33, L15108, doi:10.1029/2006GL026161.

Jones Jr., M., J. M. Forbes, M. E. Hagan, and A. Maute (2013), Non-migrating tides in the ionosphere-thermosphere: In situ versus tropospheric sources, *J. Geophys. Res. Space Physics*, 118, 2438–2451, doi:10.1002/jgra.50257.

Kil, H., W. K. Lee, J. Shim, L. J. Paxton, and Y. Zhang (2013), The effect of the 135.6 nm emission originated from the ionosphere on the TIMED/GUVI O/N_2 ratio, *J. Geophys. Res. Space Physics*, 118, 859–865, doi:10.1029/2012JA018112.

Kil, H., and L. J. Paxton (2011), The origin of the nonmigrating tidal structure in the column number density ratio of atomic oxygen to molecular nitrogen, *Geophys. Res. Lett.*, 38, L19108, doi:10.1029/2011GL049432.

Lewis, R. M., V. Torczon, M. W. Trosset (2000), Direct search methods: then and now, *Journal of Computational and Applied Mathematics*, 124, 191-207, doi:10.1016/S0377-0427(00)00423-4.

Li, X., W. Wan, Z. Ren, L. Liu, and B. Ning (2015), The variability of nonmigrating tides detected from TIMED/SABER observations, *J. Geophys. Res. Space Physics*, 120, 10,793–10,808, doi:10.1002/2015JA021577.

Lieberman, R. S. (1991), Nonmigrating diurnal tides in the equatorial middle atmosphere, J. *Atmos. Sci.*, 48, 1112-1123, doi:10.1175/1520-0469(1991)048<1112:NDTITE>2.0.CO;2.

Lieberman, R. S., J. Oberheide, and E. R. Talaat (2013), Nonmigrating diurnal tides observed in global thermospheric winds, *J. Geophys. Res. Space Physics*, 118, 7384–7397, doi:10.1002/2013JA018975.

Maute, A. (2017). Thermosphere-ionosphere-electrodynamics general circulation model for the ionospheric connection explorer: TIEGCM-ICON. *Space Science Reviews*, 212(1-2), 523–551. https://doi.org/10.1007/s11214-017-0330-3.

McClintock, W. E., Eastes, R. W., Hoskins, A. C., Siegmund, O. H. W., McPhate, J. B., Krywonos, A., et al. (2020a). Global-scale observations of the limb and disk mission implementation: 1. Instrument design and early flight performance. *Journal of Geophysical Research: Space Physics, 125*, e2020JA027797. https://doi.org/10.1029/2020JA027797.

McClintock, W. E., Eastes, R. W., Beland, S., Bryant, K. B., Burns, A. G., Correira, J., et al. (2020b). Global-scale observations of the limb and disk mission implementation: 2. Observations, data pipeline, and level 1 data products. *Journal of Geophysical Research: Space Physics, 125*, e2020JA027809. https://doi.org/10.1029/2020JA027809.

Nischal, N., Oberheide, J., Mlynczak, M. G., Marsh, D. R., & Gan, Q. (2019). Solar cycle variability of nonmigrating tides in the 5.3 and 15 μm infrared cooling of the thermosphere (100–

150 km) from SABER. *Journal of Geophysical Research: Space Physics*, 124, 2338–2356. https://doi.org/10.1029/2018JA026356.

Oberheide, J., J. M. Forbes, X. Zhang, and S. L. Bruinsma (2011), Climatology of upward propagating diurnal and semidiurnal tides in the thermosphere, *J. Geophys. Res.*, 116, A11306, doi:10.1029/2011JA016784.

Oberheide, J., M. E. Hagan, R. G. Roble, and D. Offermann (2002), Sources of nonmigrating tides in the tropical middle atmosphere, *J. Geophys. Res.*, 107(D21), 4567, doi:10.1029/2002JD002220.

Oberheide, J., M. G. Mlynczak, C. N. Mosso, B. M. Schroeder, B. Funke, and A. Maute (2013), Impact of tropospheric tides on the nitric oxide 5.3 μm infrared cooling of the low-latitude thermosphere during solar minimum conditions, *J. Geophys. Res. Space Physics*, 118, 7283–7293, doi:10.1002/2013JA019278.

Oberheide, J., Pedatella, N. M., Gan, Q., Kumari, K., Burns, A. G., & Eastes, R. (2020). Thermospheric composition O/N_2 response to an altered meridional mean circulation during Sudden Stratospheric Warmings observed by GOLD. *Geophysical Research Letters*, 47, e2019GL086313. https://doi.org/10.1029/2019GL086313.

Pedatella, N. M., J. Oberheide, E. K. Sutton, H.-L. Liu, J. L. Anderson, and K. Raeder (2016), Short-term nonmigrating tide variability in the mesosphere, thermosphere, and ionosphere, J. Geophys. Res. Space Physics, 121, 3621–3633, doi:10.1002/2016JA022528.

Strickland, D. J., J. S. Evans, and L. J. Paxton (1995), Satellite remote sensing of thermospheric O/N_2 and solar EUV: 1. Theory, *J. Geophys. Res.*, 100, 12,217–12,226, doi:10.1029/95JA00574.

Ward, W. E., et al. (2010), On the consistency of model, ground-based, and satellite observations of tidal signatures: Initial results from the CAWSES tidal campaigns, J. *Geophys. Res.*, 115, D07107, doi:10.1029/2009JD012593.

Zhang, X., J. M. Forbes, and M. E. Hagan (2010a), Longitudinal variation of tides in the MLT region: 1. Tides driven by tropospheric net radiative heating, *J. Geophys. Res.*, 115, A06316, doi:10.1029/2009JA014897.

Zhang, X., J. M. Forbes, and M. E. Hagan (2010b), Longitudinal variation of tides in the MLT region: 2. Relative effects of solar radiative and latent heating, *J. Geophys. Res.*, 115, A06317, doi:10.1029/2009JA014898.

Zhang, X., J. M. Forbes, M. E. Hagan, J. M. Russell III, S. E. Palo, C. J. Mertens, and M. G. Mlynczak (2006), Monthly tidal temperatures 20–120 km from TIMED/SABER, *J. Geophys. Res.*, 111, A10S08, doi:10.1029/2005JA011504.